



Cite this: RSC Adv., 2015, 5, 17541

Composite mesoporous silica nanoparticle/chitosan nanofibers for bone tissue engineering

Kai Li,^{†[a](#)} Hailang Sun,^{†[b](#)} Haitao Sui,^c Yongxing Zhang,^a He Liang,^a Xiaofeng Wu^{*a} and Qinghua Zhao^{*a}

Electrospinning of inorganic–organic composites into nanofibers has emerged as a new approach for fabricating scaffolds for biomimetically engineered bone tissues. This paper reports novel biomimetic nanocomposite nanofibers composed of mesoporous silica nanoparticles/chitosan (MSN/CTS) prepared by electrospinning. The optimal conditions for electrospinning CTS and MSNs were identified to produce beadless nanofibers without any aggregation of the MSNs. The mechanical properties of the composite scaffolds were analyzed by tensile tests for scaffolds with varying contents of MSNs within CTS fibers. Increasing the MSN content to 10 wt% enhanced the mechanical properties of the composite scaffolds, whereas increasing the content beyond 10 wt% disrupted the polymer chain networks within the CTS nanofibers and weakened the mechanical strength of the fibers. Swelling ratio, shrinkage and biodegradation properties were characterized. MTT, SEM, alkaline phosphatase activity and Alizarin Red staining analysis of osteoblast-cultured scaffolds confirmed the biocompatibility and functionally promoted biomaterialization of the composite scaffolds. Thus, the prepared MSN/CTS composite nanofibrous mats are highly promising as local implantable scaffolds for potential bone tissue engineering applications.

Received 25th November 2014
Accepted 3rd February 2015

DOI: 10.1039/c4ra15232h
www.rsc.org/advances

Introduction

Chitosan (CTS), which is the only natural cationic polysaccharide possessing a chemical structure similar to that of extracellular glycosaminoglycan, exhibit excellent biocompatibility, biodegradability and biological activity.¹ Recent studies show that electrospun nanofiber scaffolds are excellent substrates for bone tissue engineering due to the relevance of topography in mimicking the ECM structure.^{2–5} CTS has been demonstrated promising performance as a scaffold material for promoting the differentiation of osteoprogenitor cells, osteoblasts cell growth and bone formation.^{6–9} Various strategies have been developed to create a three-dimensional (3D) CTS structure with high porosity and osteoconductivity. To mimic bone, ECM consisting of organic components such as collagen as well as inorganic components such as hydroxyapatite, the incorporation of ceramic components into CTS scaffolds has also been demonstrated.¹⁰ Furthermore, to resemble natural

tissues such as collagen and high interconnectivity structure, fibrous CTS scaffolds have also been constructed using electrospinning for bone regeneration.^{11,12} However, fibrous CTS scaffolds are significantly weak to physical loading compared to Bio-Gide membranes, which are the commonly used membranes for guiding bone regeneration in clinical settings.^{13,14} Thus, in an attempt to use fibrous CTS scaffolds to sustain tensional or compressional stresses in bone tissue engineering, enhancing the mechanical properties of scaffolds is greatly desired. The hybridization of CTS with bioactive inorganic materials, such as hydroxyapatite, tricalcium phosphate, carbon nanotube, silica xerogel and bioactive glass, is regarded as an appropriate method for overcoming the weaknesses of CTS and still retaining its osteogenesis characteristic.^{15–20} Hence, a blend of bioactive inorganic materials/CTS should be a feasible approach to develop a composite scaffold for bone tissue engineering considering both the biomechanical and tissue regeneration capabilities of the scaffold.

Mesoporous silica nanoparticles (MSNs) are a class of bioactive inorganic materials with a honey comb-like structure and controllable pore sizes, high surface areas, high pore volumes and homogeneous nanoscale structures that have received little attention as reinforcement agents in polymers for bone tissue engineering scaffold applications.²¹ The highly porous nature of MSNs indicates that mechanical interlocking could occur between the particles and a given polymer to form strong bonds that could mitigate interfacial adhesion problems

^aDepartment of orthopaedics, Shanghai First People's Hospital, School of Medicine, Shanghai Jiao Tong University, Shanghai 200080, P. R. China. E-mail: sawboneszhao@163.com; wuxfeng74@gmail.com; Fax: +86-21-37798591; Tel: +86-21-63241377

^bDepartment of Orthopaedics, Huai'an First people's hospital, Nanjing Medical University, Huai'an 223300, P. R. China

^cDepartment of Orthopaedics, Dongying people's hospital, Dongying, ShanDong, 257000, P. R. China

† K. Li and H. Sun contributed equally to this work.

typically observed with other types of reinforcement materials. In addition, the high surface area inherent to MSNs could lead to an efficient stress transfer mechanism, thus increasing the strength of MSN/polymer composites.²² Although MSN-embedded electrospun fiber mats have been previously reported for PLGA or PLLA nanofibers used for drug delivery,^{23,24} there was no investigations on CTS nanofibers containing MSNs for bone tissue engineering.

Thus, in the present work, we report the fabrication of a novel multifunctional hybrid nanofibrous scaffold comprising MSNs and CTS. This design not only mimics the extracellular matrix milieu of a nanofibrous network but also incorporates bioactive ceramic MSNs that can aid cell adhesion, proliferation, and biomimetic mineralization of bone cells. The effect of MSNs on the morphology and mechanical properties of the nanofiber scaffolds was also investigated.

Experimental

Materials

Chitosan (CTS, DD > 85%) derived from crab shells, dimethyl sulfoxide (DMSO, 99C%) tetraethylorthosilicate (TEOS), and cetyltrimethylammonium bromide (CTAB) were purchased from Sigma Aldrich. Poly(ethylene oxide) with a molecular weight >5 000 000 Da (UHMWPEO) was supplied by Avocado. All other chemicals were of analytical grade and obtained from Sinopharm Chemical Reagent Co. Ltd.

Synthesis of MSNs

The procedure employed to synthesize MSNs was as follows.²⁵ Briefly, 1.82 g of CTAB and 3.0 g of NH₄F were dissolved in 500 mL of distilled water, then heated to 80 °C in an oil bath and stirred for 1 h. Nine milliliters of TEOS was subsequently added dropwise to the solution over a period of approximately 16 min. After the resulting solution was stirred for 2 h, the product was collected by centrifugation at 10 000 rpm for 15 min and washed thoroughly with distilled water and ethanol. The surfactants were removed by extraction three times in a mixture

of 200 mL of ethanol and 4 mL of hydrochloric acid (36–38%) at 80 °C for 12 h. Finally, the resultant powders were dried under vacuum for further use.

Preparation of MSN/CTS composite nanofibers

The prepared MSNs were subsequently incorporated into CTS nanofibers using blend electrospinning, and the MSN contents in the MSN/CTS composite nanofibers were 10% and 20%. In a typical procedure, CTS powder was dissolved with 15 wt% ultrahigh molecular weight poly(ethylene oxide) (relative to the CTS content) in an aqueous solvent system composed of 3 wt% acetic acid and dimethyl sulfoxide (10 : 1, w/w) under gentle stirring for 24 h. MSNs was added to the CTS solution and stirred thoroughly to form a homogeneous blend for subsequent electrospinning. The solution was filled into a 5.0 mL plastic syringe with an 18 gauge blunt-ended needle, and the distance between the needle and the aluminum foil collector was 15 cm. The syringe was loaded in a syringe pump (KDS100, KD Scientific) and dispensed at a rate of 1 mL h⁻¹ at an applied voltage of 16 kV using a high-voltage power supply (TXR1020N30-30, TESLAMAN Co. Ltd). The collected nanofibers were vacuum dried for at least 72 h to remove the residual solvent before further use.

Characterization

The surface morphologies of the MSNs and electrospun mats were observed using a field emission scanning electron microscope (FESEM, Hitachi S-4800, Japan) and a scanning electron microscope (SEM, Hitachi TM-1000, Japan), respectively. The distribution of MSNs embedded in the CTS nanofibers was observed using a transmission electron microscope (TEM, Hitachi H-800, Japan) at an operating voltage of 200 kV; the fibers were mounted onto a copper/carbon grid for observation.

The particle size distribution was determined by dynamic light scattering (DLS) measurements using a Malvern Zetasizer Nano ZS model ZEN3600 (Worcestershire, UK). Nitrogen adsorption-desorption isotherms were measured with a

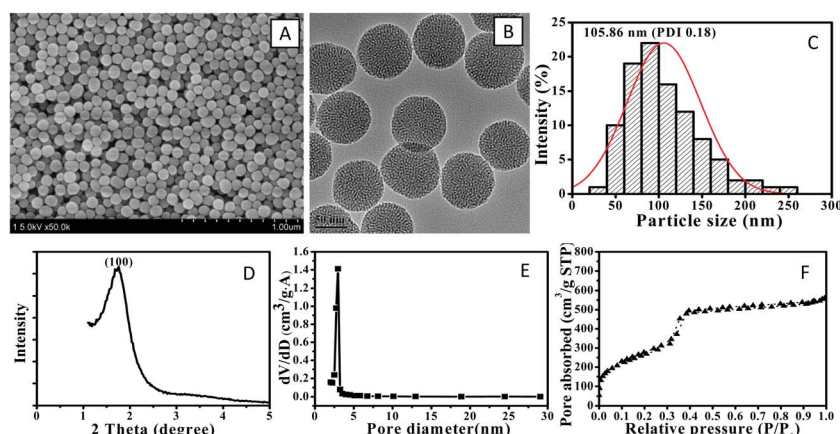


Fig. 1 (A) SEM and (B) TEM images of MSNs. (C) Size distribution of MSNs measured by the DLS method. (D) XRD patterns of MSNs. (E) Pore size distribution of MSNs. (F) Nitrogen adsorption-desorption isotherms of MSNs.

Micromeritics Tristar II analyzer (Micromeritics, USA) at liquid nitrogen temperature under a continuous adsorption condition. The average pore size distributions of MSNs were determined from the desorption branches of the isotherms by the Barrett–Joyner–Halenda (BJH) method, and the specific surface area of the fibers was calculated according to the Brunauer–Emmett–Teller (BET) method.

The average diameter of the nanofibers was obtained from at least 50 measurements conducted on a typical FESEM image using ImageJ software (NIH, USA).

Tensile testing of MSN/CTS hybrid scaffolds was conducted based on the ASTM D882 standard test method using a Universal Testing Machine (H5K-S, Hounsfield, United Kingdom) equipped with a 10 N load cell. Rectangular specimens ($50 \times 10 \times 0.10\text{--}0.15$ mm) were strained at a constant cross-head speed of 10 mm min^{-1} .

Swelling behaviors of CTS and 10 wt% MSN/CTS nanofibers were studied to assess their relative stability under aqueous medium. For swelling study, sample mats (1×1 cm) were incubated in PBS (pH 7.4) at 37°C for 12 h. After incubation, samples were removed at different time points, wiped gently to remove the surface liquid and sample weights were measured (W_w). Samples were air-dried and further weighed (W_d). The swelling ratio (S_w) of samples ($n = 3$) was calculated using following equation: $S_w = (W_w - W_d)/W_d \times 100\%$.

For the shrinkage test, three samples (1×1 cm) from each group were recovered after 12 h of incubation and subsequently put in a vacuum oven to completely remove the water. The sizes

of the dried samples were measured and compared with the initial dimension. The *in vitro* shrinkage percentages of samples were defined as the ratio of the surface dimensional changes of the recovered membrane. And then were sputter-coated with a layer of gold for observation by SEM (JEOL JSM-5600LV, Japan).

In vitro degradation behaviors of CTS and MSN/CTS nanofibers were evaluated in lysozyme medium for 3 weeks following a procedure modified from a published protocol.²⁶ The test membranes were separately immersed in 1 mg mL^{-1} lysozyme solutions (pH 7.4) and incubated at 37°C . Then, the degraded samples were rinsed with PBS for 3 times, and air-dried for recording their final weight (W_f). The weight loss of each sample was calculated according to the equation: Weight Loss (%) = $(W_i - W_f)/W_i$, where W_i denotes the initial weight of the sample in its dry state prior to submersion in PBS. Also, the degraded scaffolds were dried, and then were sputter-coated with a layer of gold for observation by SEM (JEOL JSM-5600LV, Japan).

Cell seeding

MC3T3-E1 osteoblasts (Shanghai institutes for biological sciences, China) were routinely cultured in 9 cm^2 cell culture dishes in a growth medium containing 89% L-DMEM (low glucose), 10% fetal bovine serum (FBS), and 1% penicillin-streptomycin. After reaching 80% confluence, cells were passaged with trypsin-EDTA. Cover glasses covered with electrospun CTS and MSN/CTS nanofibrous meshes were placed in 24-well plates (JET-BIOFIL) and treated as previously study

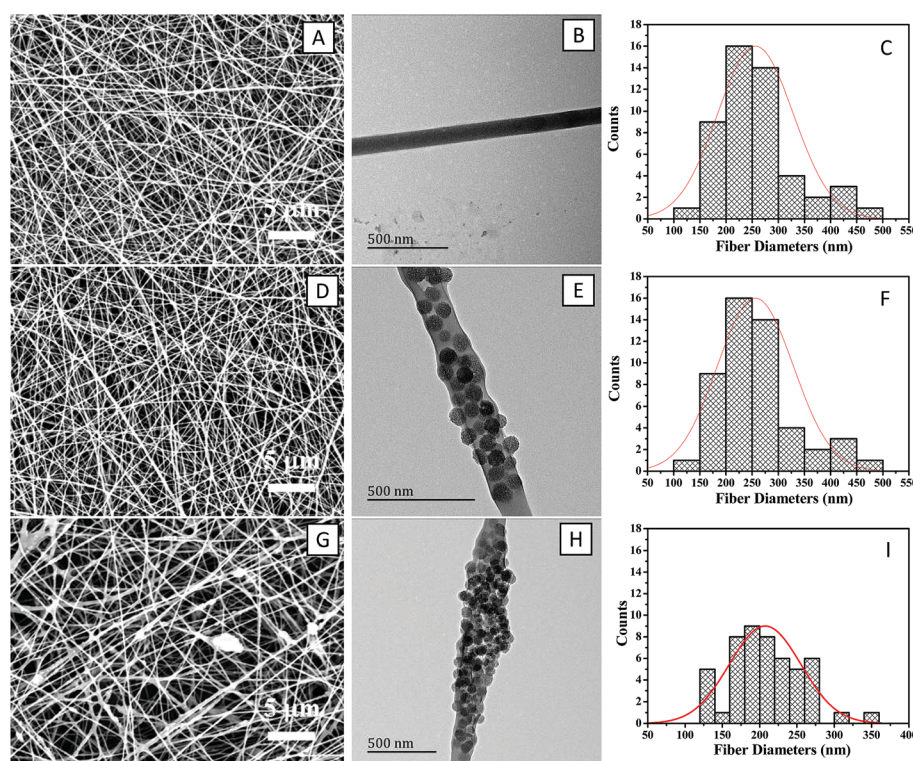


Fig. 2 SEM and TEM images of (A and B) CTS electrospun mat, (D and E) 10% MSN/CTS electrospun mat, and (G and H) 20% MSN/CTS electrospun mat and the corresponding diameter distributions (C, F and I).

described.¹⁹ A cell suspension were then seeded onto the nanofibrous scaffolds in the 24-well plates at cellular densities of 5×10^4 per well.

Cell morphology

To observe the cell morphology, cell-scaffold constructs were washed with PBS to remove non-adherent cells and fixed with 4% paraformaldehyde for 3 h at room temperature. The constructs were further dehydrated using a series of graded alcohol solutions and finally dried overnight. After coating with gold, the dried cellular constructs were observed by SEM (Hitachi TM-1000, Tokyo, Japan) at an accelerating voltage of 10 kV.

Cell proliferation

Cell proliferation was evaluated by an MTT (3-(4,5-dimethylthiazol-2-yl)-2,5-diphenyltetrazolium bromide, a yellow tetrazole) assay. Briefly, at predetermined intervals of incubation, the medium on the samples was removed and washed with PBS three times, and then 500 μ L of medium and 50 μ L of 5 mg mL⁻¹ MTT were added to each well containing MC3T3-E1 osteoblasts. The plate was then incubated at 37 °C in a humidified atmosphere of 5% CO₂ for 4 h, followed by the removal of the mixed solution of medium and MTT and the addition of 400 μ L of DMSO to each well, pipetting up and down to dissolve crystals in the dark. Finally, the solutions were transferred to a microplate reader (MK3, Thermo, USA) for absorbance measurements at 492 nm.

Alkaline phosphatase (ALP) activity

ALP activity was assayed using a BCIP/NBT alkaline phosphatase color development kit (Nanjing Jiancheng Bioengineering

Institute) according to the manufacturer's instructions. Membrane scaffolds were seeded with MC3T3-E1 osteoblasts at a density of 5×10^4 cells per well in 24-well plates. Briefly, cell-scaffold constructs were washed three times with PBS and 50 mL of cold 10 mM Tris/HCl buffer (pH 7.4) containing 0.1% Triton X-100 added prior to incubation at 4 °C overnight. A 100 μ L volume of ALP substrate solution (2 mM MgCl₂ and 16 mM *p*-nitrophenyl phosphate) was then mixed with each sample. After incubation at 37 °C for 30 min, the reaction was terminated by the addition of 50 mL of 0.2 M NaOH, and the liberated *p*-nitrophenol was measured spectrophotometrically at 405 nm. By normalizing to the cell number determined from the MTT assay, the specific ALP activity per cell basis was reported and expressed as OD405/OD492.

Mineralization assay

Cell-membrane scaffolds were subjected to Alizarin Red Staining (ARS) to determine the calcium content at 7 and 14 d of culture after binding mineralized calcium salts to the membrane scaffolds. Membrane scaffolds were washed three times with PBS and fixed with 2.5% glutaraldehyde solution (dissolved in 0.1 M phosphate buffer) for 2 h. In 25 mL of deionized water, 0.5 g of ARS was dissolved, and the pH was adjusted to 4.1–4.3 with 10% ammonium hydroxide. Two hundred microliters of ARS solution was added to each well, followed by incubation for 2 min at room temperature. Deionized water was used to wash off the excess dye adsorbed on the membrane scaffold surface. The presence of mineral deposits was qualitatively evaluated based on the intensity of red color observed on the scaffold surface in photomicrographs obtained using an inverted microscope (Nikon Eclipse TE 2000-U, AVON,

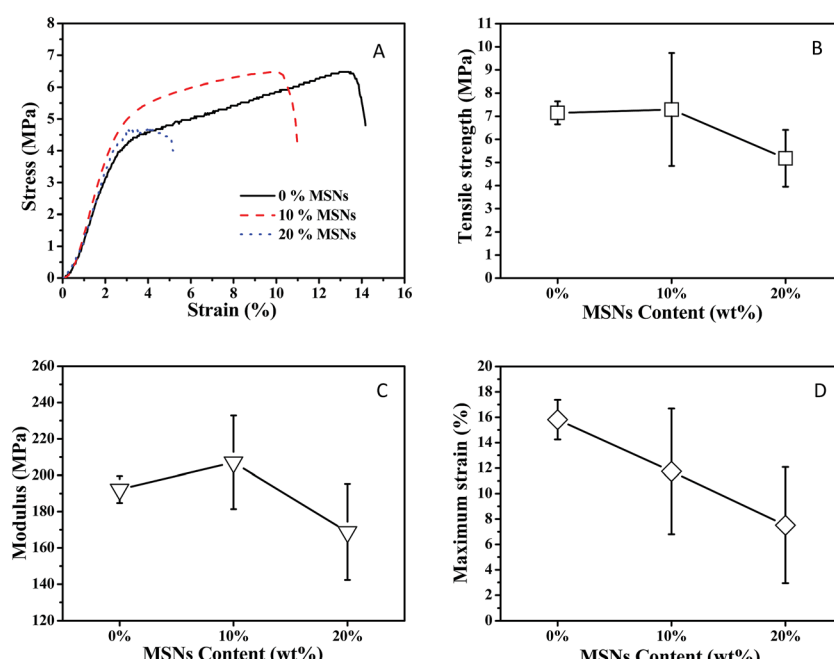


Fig. 3 (A) Typical tensile stress–strain curves of MSN/CTS composite nanofibers with different MSN contents. Effects of MSN content on (B) tensile strength, (C) Young's modulus, and (D) maximum strain of MSN/CTS composite scaffolds.

MA). The calcium content was quantified using cetylpyridinium chloride (CPC) treatment. ARS-stained membrane scaffolds were washed with deionized water and followed by treatment with 1 mL of 10% CPC solution for 1 h to desorb calcium ions. The absorbance of the solution was read at 540 nm in a spectrophotometer (OD540) and normalized to the cell number from the MTT assay (OD540/OD492).

Statistical analysis

Each value was expressed as the mean \pm standard error of at least three samples. Statistical analysis was performed using the unpaired Student's *t*-test. A value of $P < 0.05$ was considered statistically significant.

Results and discussion

Morphology and structure of MSNs

The morphology and structure of the MSNs were analyzed using a series of techniques, including FESEM, TEM, DLS and nitrogen adsorption–desorption isotherm analysis. SEM images showed that the MSNs were highly monodisperse and spherical (Fig. 1A). TEM imaging clearly revealed a wormlike pore structure and highly ordered mesoporous channels within the pores of the MSNs (Fig. 1B). As shown in Fig. 1C, the mesoporous spheres were uniform in size, with a hydrodynamic size of 105.86 nm and polydispersity index (PDI) of 0.18 measured by

DLS, indicating a relatively narrow particle size distribution. The XRD patterns of the MSNs exhibit a well-resolved diffraction peak at approximately 2° that can be indexed to the (100) diffraction plane associated with $p6mm$ hexagonal symmetry,²⁷ suggesting the existence of a partially ordered mesostructure (Fig. 1D). As depicted in Fig. 1E and F, the isotherm of the MSNs showed IV curves typical of a mesoporous material,²⁸ with a well-defined capillary condensation step and a narrow pore size distribution; these findings further confirmed the existence of uniform mesopores. N^2 adsorption–desorption analysis also revealed that the MSNs possessed a BET surface area of 561.03 $m^2 g^{-1}$ and a pore size of 2.78 nm. These results indicate that the synthesized silica nanoparticles possessed a reasonably small size suitable for incorporation into polymer nanofibers.

Morphology of MSN/CTS composite electrospun fibers

The morphology and diameter distribution of the MSN/CTS composite electrospun fibers are shown in Fig. 2. Fig. 2A and B clearly shows that the surface of the CTS electrospun fibers was smooth, and no MSNs were observed. However, the surface of the MSN-loaded electrospun fibers became rough, with many protrusions clearly observed on the surface of the fibers (Fig. 2D, E, G and H). In particular, agglomeration of the MSNs could be observed when the amount of MSNs added reached up to 20%, which is similar to the results reported by Song *et al.*²⁴ TEM images also showed that the silica spheres were well

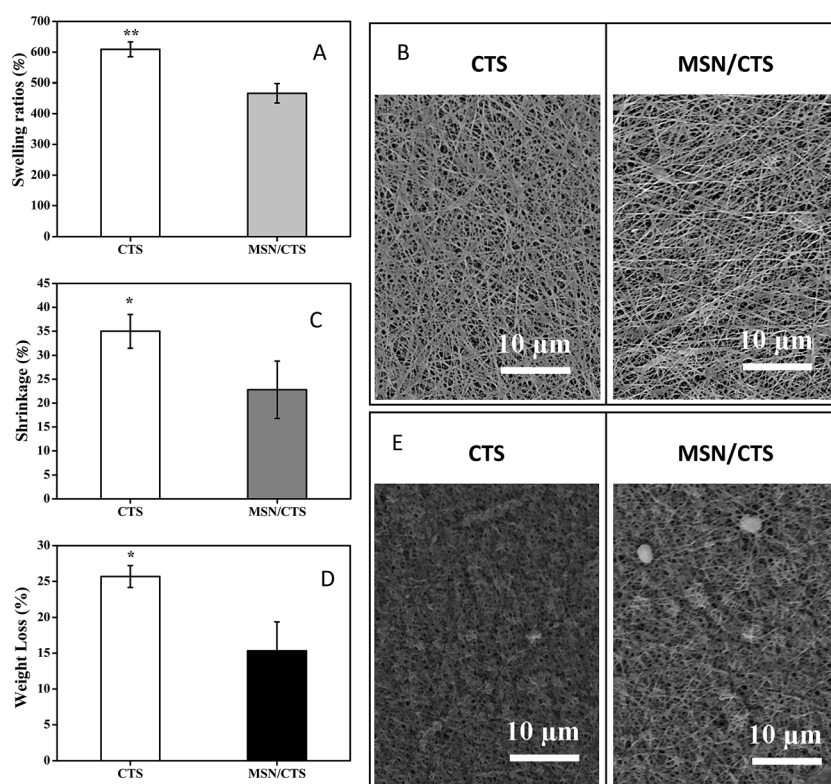


Fig. 4 Swelling ratio (A), SEM images (B) and shrinkage (C) of CTS and MSN/CTS nanofibers after being soaked in PBS for 12 h. Degradation degree (D) and SEM images (E) of CTS and MSN/CTS nanofibers after subject to lysozyme degradation for 3 weeks. Data are presented as mean \pm standard deviation with $n = 3$ (* $P < 0.05$, ** $P < 0.01$).

distributed within the composite fibers when the content of MSNs was lower than 10 wt%, and some MSNs were positioned near the surface of the fibers, forming the protrusions. Additionally, the average diameter of the MSN/CTS electrospun fibers increased with the increase in the MSN content to 10% (207 ± 48 nm) and 15% (256 ± 73 nm), reaching diameters larger than those of the CTS fibers (179 ± 42 nm); this increase in diameter was related to the increase in the viscosity of the solution with the content of MSNs, which led to a lower extent of stretching for the polymer solution and an increase in the diameter of the electrospun fibers.

Mechanical properties of hybrid scaffolds

Tensile tests were conducted on the composite scaffolds composed of CTS fibroin and MSNs. Interestingly, all of the mechanical properties of the scaffolds (except for the maximum strain) increased when the MSN concentration was lower than 10 wt% and then decreased at higher MSN contents (Fig. 3A–C). Unlike the other properties, the maximum strain of the composite scaffolds decreased with the content of MSNs (Fig. 3D). The initial improvement in the mechanical properties was attributed to the stiffness of the MSNs, which reduced the flexibility of CTS. However, when the amount of MSNs

exceeded the critical volume fraction for aggregation, the MSNs introduced disruption and functioned as discontinuities among fiber chains because the distance between the particles decreased and the toughness substantially decreased.^{29,30} Thus, an increase of MSNs content in CTS fibers directly caused such accelerated breakage of scaffolds during tensile tests. Hence, the optimal concentration of MSNs was 10 wt%, which facilitated the production of composite nanofibers with homogenously dispersed MSNs and the highest mechanical properties.

Swelling and biodegradation properties

The swelling study of CTS and 10 wt% MSN/CTS nanofibers revealed swelling ratios in PBS medium with more than 600% and 400% weight gain, respectively (Fig. 4A). And the morphology of MSN/CTS nanofibers remained better fiber shape after being soaked in PBS for 12 h (Fig. 4B). These may be attributed to higher stability rendered by MSNs.

Containing hydrophilic groups, CTS was expected to swell in water and thus prevent the shrinkage of the electrospun membrane. However, electrospun CTS membrane shrunk to $35.0 \pm 3.5\%$ of its original size after immersing in PBS for 12 h, and $22.8 \pm 6\%$ shrinkage was observed in the MSN/CTS

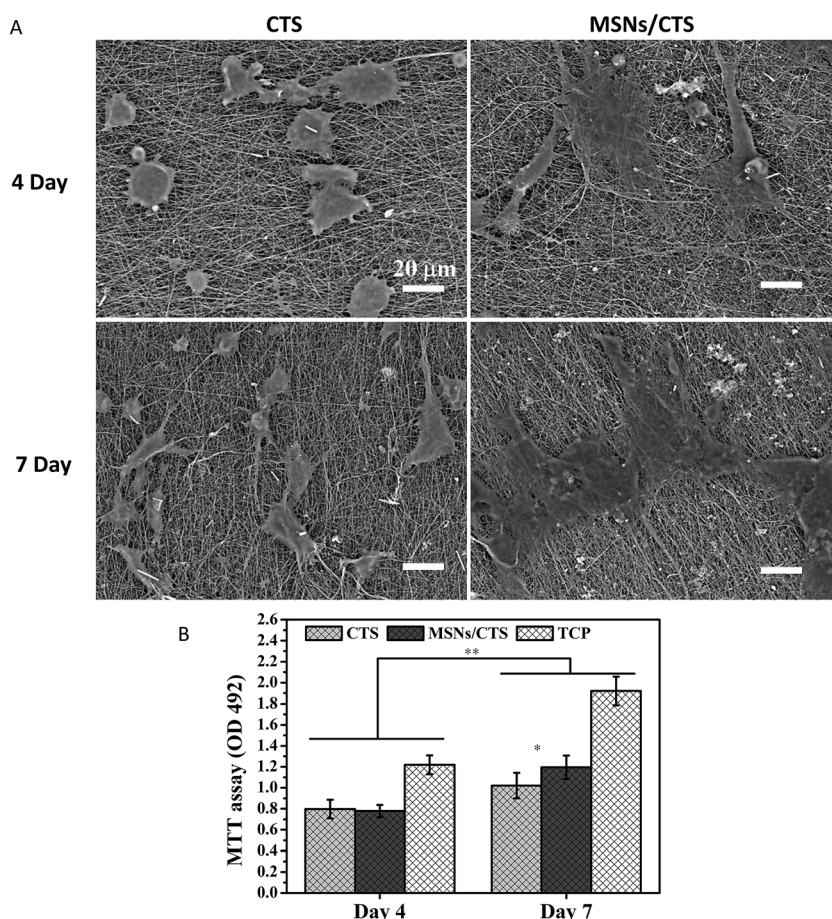


Fig. 5 (A) Morphology of osteoblasts cultured on electrospun nanofibrous scaffolds of CTS and MSN/CTS at 4 and 7 d, respectively. (B) Histogram of osteoblast proliferation by MTT assay. * $p < 0.05$, ** $p < 0.01$.

composite membrane (Fig. 4C). It was probably because CTS/PEO component was dissolved.^{31,32}

In vitro biodegradation of as-spun CTS and 10 wt% MSN/CTS nanofibers were carried out in aqueous medium supplemented with lysozyme. It was observed that both the samples (CTS and MSN/CTS) were degradable under simulated condition (37 °C, pH 7.4). After 3 weeks of incubation in lysozyme medium, the weight losing for CTS and MSN/CTS nanofiber mats were $25.67 \pm 1.53\%$ and $15.33 \pm 4.04\%$ (Fig. 4D), respectively. Clearly, MSN/CTS nanofiber mats possessed significantly lower degradation degree when compared with that of CTS nanofibers. This is also consistent with SEM observation in that the MSN/CTS nanofiber membranes retained their fibrous structure, while CTS nanofibers became fuzzy and mussy (Fig. 4E). It is known that the degradation function of lysozyme on CTS is strongly dependent on the acetylated unit in CTS molecular structure.³³ It may be owing to intramolecular and intermolecular structures or other more complicated structures may be formed by the incorporation of MSN, which could prevent the combination between lysozyme and N-acetylglucosamine residue of the CTS chains.

Take together above all, the MSN/CTS nanofiber mat with high water retention capacity, stability and biodegradability may be considered as potential scaffold for tissue engineering.

Cellular morphology and proliferation

To determine the ability of the scaffolds to support cell adhesion and proliferation, we seeded MC3T3-E1 osteoblasts on CTS

and MSN/CTS (10 wt%) scaffolds and then examined the morphology of the osteoblasts by SEM at 4 d and 7 d; furthermore, we measured the cells' proliferation ability by an MTT assay. Cell spreading on materials is related to filopodia extension and affects cell functions, including proliferation and differentiation.³⁴ SEM micrographs indicated that most of the MC3T3-E1 osteoblasts were spherical on the CTS scaffolds, whereas they exhibited a polygonal morphology on the MSN/CTS scaffolds (Fig. 5A). Therefore, MSN-containing CTS nanofibers facilitate an adequate environment for cell growth and production of ECM. The number of cells on the nanofibrous scaffolds increased with increasing culture time³⁵ but exhibits an effect of nanofiber composition on cell proliferation rate. At day 4, the viable cell number was not significant different among nanofibers. However, from day 7, a significant difference ($p < 0.05$) in cell number was observed between CTS and MSN/CTS nanofibers. (Fig. 5B). Clearly, the MC3T3-E1 osteoblasts preferentially adhered, spread and grew on the MSN/CTS nanofibrous scaffolds, likely because the nanofibrous, porous morphology and the high specific surface area of the scaffolds facilitated the adsorption of growth factors and tissue oxygenation resulted in enhanced cell adhesion, spreading and proliferation.

Alkaline phosphatase (ALP) activity

ALP is regarded as a key marker associated with fully mature, differentiating osteoblasts.³⁶ The results obtained from the ALP

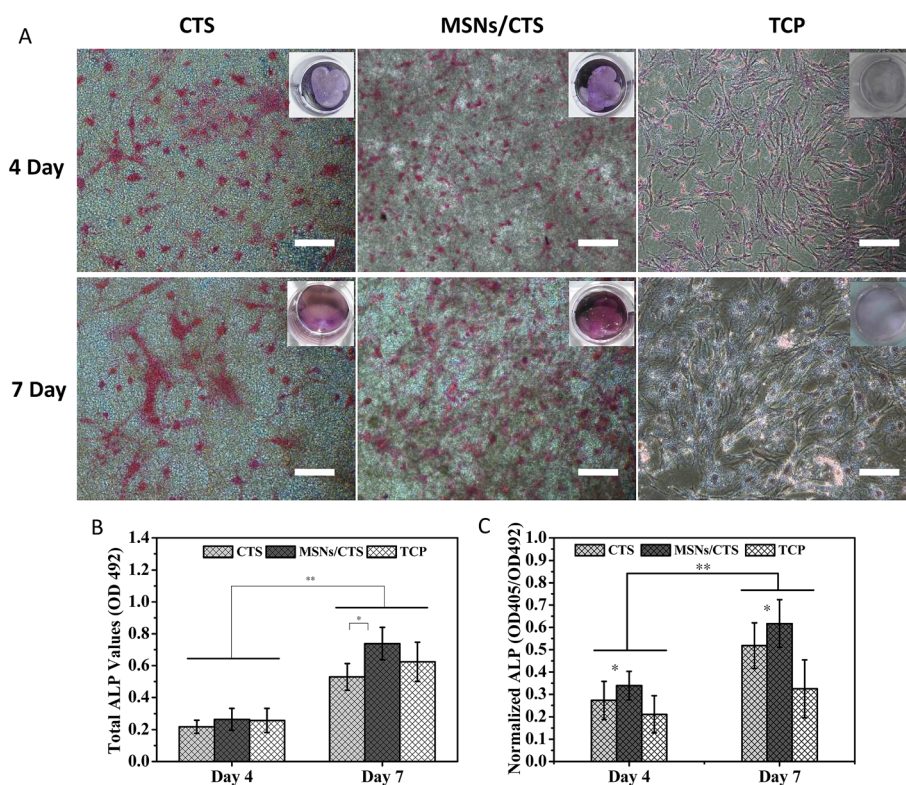


Fig. 6 (A) ALP staining of osteoblasts attached to electrospun fibrous CTS, MSNs/CTS and TCP scaffolds after 4 and 7 d of culture. Insets show macroscopic appearance. (B) Quantitatively measured ALP activity and (C) normalized ALP activity of osteoblasts cultured on scaffolds. Scale bar = 100 μ m. * $p < 0.05$, ** $p < 0.01$.

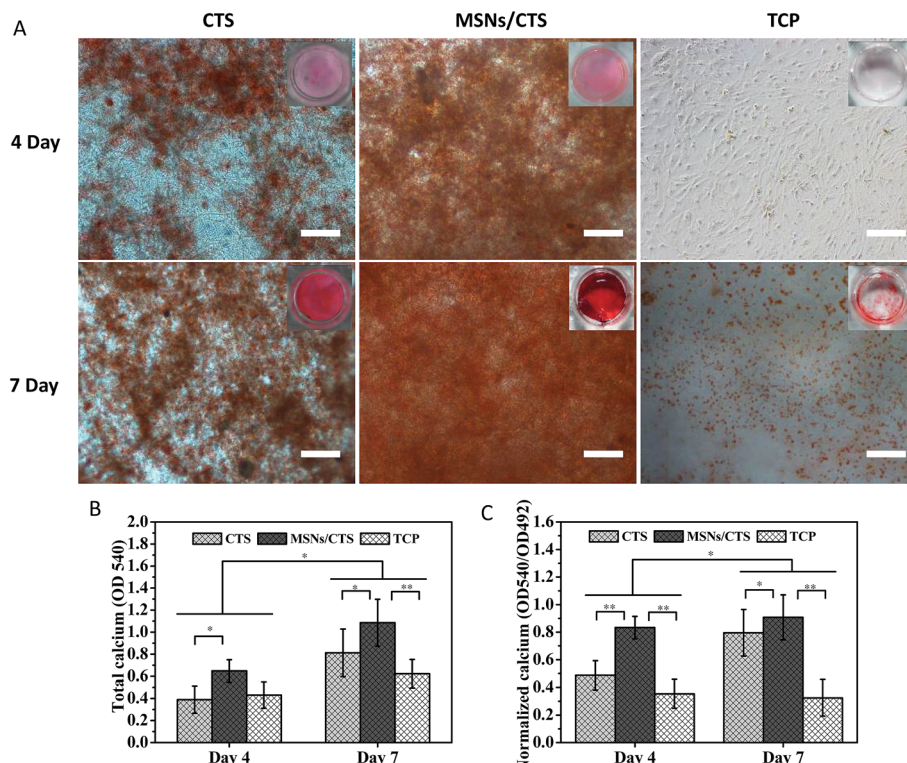


Fig. 7 Alizarin red staining of osteoblasts cultured on electrospun CTS, MSN/CTS and TCP scaffolds after 4 and 7 days of culture. Insets show macroscopic appearance. (B) Quantitatively determined mineral deposition based on total (B) and normalized (C) calcium content of osteoblasts cultured on scaffolds. Scale bar = 100 μ m. * $p < 0.05$, ** $p < 0.01$.

staining of MC3T3-E1 osteoblasts cultured on CTS and MSN/CTS membrane scaffolds monitored after 4 and 7 d of cell seeding are shown in Fig. 6A. The results indicate a positive effect of the nanofibrous MSN/CTS scaffolds on osteogenic differentiation. Osteoblasts cultured on the MSN/CTS nanofibers exhibited significantly higher ALP activity than those cultured on the CTS and TCP fibers. Quantitative measurements of the ALP activity revealed that on day 4 of culture, there was no significant difference in OD values between the CTS and MSN/CTS scaffolds, but a significant difference was observed on day 7 (Fig. 6B). The normalized ALP values corresponding to cell number are presented in Fig. 6C. With respect to these normalized values, in contrast to the total ALP values, a significant difference was observed between the MSN/CTS group and the CTS and TCP groups from day 4 to 7. The high levels of ALP activity observed on the MSN/CTS scaffolds indicate the scaffold's ability to support osteoblast maturation.

Mineralization

Mineralization is the process by which calcium phosphate deposits on the surface of substrates.^{36,37} Anionic matrix molecules will take up Ca^{2+} , followed by phosphate ions, thus leading to calcification through nucleation and growth when osteoblasts differentiate on nanofibers. ARS can bind to Ca^{2+} in mineralized ECM and thereby show bright red stains.³⁸ Fig. 7A shows optical microscopy images of ARS-stained CTS and MSN/CTS membrane scaffolds, confirming the variations in stain

intensity for different membrane scaffolds with respect to time. At day 4, the Alizarin Red stain showed reddish dots on both the CTS and MSN/CTS membrane scaffolds, but almost no positive stains were observed over the TCP scaffolds. Significantly enhanced staining was observed at day 7 for the TCP, CTS and MSN/CTS scaffolds. The MSN/CTS membrane scaffolds showed the highest intensity of red staining and were able to induce osteogenic differentiation, making them suitable for bone regeneration applications. Quantitative mineralization measurements were also performed after extracting ARS with 10% CPC to evaluate the calcium-rich mineral deposits of osteoblasts (Fig. 7B). Calcium deposition was recorded as total calcium content *versus* culture period, and the quantitative data were then normalized with respect to cell number (Fig. 7C). The total calcium content was observed to increase with time. At day 7, the total calcium content in the deposited minerals on the MSN nanofibers was significantly higher than that of the CTS and TCP scaffolds, which was attributed to the release of constitutive ions from the MSNs.³⁹

Conclusion

Electrospun MSN/CTS nanofibrous membrane scaffolds were fabricated by the electrospinning technique. The MSN/CTS ratios were varied to investigate the effect of the MSN content on the morphology, mechanical properties, swelling behaviors, shrinkage, biodegradation properties and biocompatibility of the composite scaffolds. The surface of the MSN/CTS nanofibers

became rougher with the increase in MSN content. Tensile testing of the composite scaffolds showed that highest strength with MSN content of 10%. MSN/CTS nanofiber mat exhibited high water retention capacity, stability and biodegradability. Further more, the MSN/CTS nanofibrous scaffolds supported osteoblast attachment, proliferation and bone formation, in addition to ALP expression and mineral deposition. Overall, biomimetic nanofibrous MSN/CTS scaffolds integrated with desired functionalities, including excellent mechanical properties, biodegradability, and bone-forming ability, show great potential for achieving optimal outcomes in the course of scaffold-assisted bone repair and in regeneration applications.

Acknowledgements

This work was financially supported by the Municipal Natural Science Foundation of Shanghai (no. 14ZR1433100). The funders had no role in study design, data collection and analysis, decision to publish, or preparation of the manuscript.

Notes and references

- B. K. Park and M.-M. Kim, *Int. J. Mol. Sci.*, 2010, **11**, 5153–5165.
- W. J. Li, C. T. Laurencin, E. J. Caterson, R. S. Tuan and F. K. Ko, *J. Biomed. Mater. Res.*, 2002, **60**, 613–621.
- Y. Zhang, C. T. Lim, S. Ramakrishna and Z. M. Huang, *J. Mater. Sci.: Mater. Med.*, 2005, **16**, 933–946.
- N. F. Huang, S. Patel, R. G. Thakar, J. Wu, B. S. Hsiao, B. Chu, R. J. Lee and S. Li, *Nano Lett.*, 2006, **6**, 537–542.
- H. Wu, J. Fan, C. Chu and J. Wu, *J. Mater. Sci.: Mater. Med.*, 2010, **21**, 3207–3215.
- T. Kawai, T. Yamada, A. Yasukawa, Y. Koyama, T. Muneta and K. Takakuda, *J. Biomed. Mater. Res., Part B*, 2009, **88**, 264–270.
- S. H. Teng, E. J. Lee, P. Wang, D. S. Shin and H. E. Kim, *J. Biomed. Mater. Res., Part B*, 2008, **87**, 132–138.
- K. Kim and J. P. Fisher, *J. Drug Targeting*, 2007, **15**, 241–252.
- A. Przekora and G. Ginalska, *Biomed. Mater.*, 2015, **10**, 015009.
- J. Venkatesan and S.-K. Kim, *Mar. Drugs*, 2010, **8**, 2252–2266.
- J. Zhao, W. Han, H. Chen, M. Tu, S. Huan, G. Miao, R. Zeng, H. Wu, Z. Cha and C. Zhou, *J. Mater. Sci.: Mater. Med.*, 2012, **23**, 517–525.
- P. Datta, S. Dhara and J. Chatterjee, *Carbohydr. Polym.*, 2012, **87**, 1354–1362.
- C. Zonggang, W. Bo, M. Xiumei, C. T. Lim, S. Ramakrishna and C. Fuzhai, *Mater. Sci. Eng., C*, 2009, **29**, 2428–2435.
- P. A. Norowski, S. Mishra, P. C. Adatrow, W. O. Haggard and J. D. Bumgardner, *J. Biomed. Mater. Res., Part A*, 2012, **100**, 2890–2896.
- W. W. Thein-Han and R. D. Misra, *Acta Biomater.*, 2009, **5**, 1182–1197.
- S. F. Wang, L. Shen, W. D. Zhang and Y. J. Tong, Preparation and mechanical properties of chitosan/carbon nanotubes composites, *Biomacromolecules*, 2005, **6**, 3067–3072.
- M. Jafarkhani, A. Fazlali, F. Moztarzadeh and M. Mozafari, *Iran. Polym. J.*, 2012, **21**, 713–720.
- E. J. Lee, D. S. Shin, H. E. Kim, H. W. Kim, Y. H. Koh and J. H. Jang, *Biomaterials*, 2009, **30**, 743–750.
- Y. Zhang, J. R. Venugopal, A. El-Turki, S. Ramakrishna, B. Su and C. T. Lim, *Biomaterials*, 2008, **29**, 4314–4322.
- S. Talebian, M. Mehrali, S. Mohan, H. Rao, B. Raghavendran, M. Mehrali, H. M. Khanlou, T. Kamarul, A. Muhammad Afifi and A. A. Abass, *RSC Adv.*, 2014, **4**, 49144–49152.
- Z. Fa-Ai, L. Dong-Keun and T. J. Pinnavaia, *Polym. Chem.*, 2010, **1**, 107–113.
- F. Shao-Yun, F. Xi-Qiao, B. Lauke and M. Yiu-Wing, *Composites, Part B*, 2008, **39**, 933–961.
- K. Qiu, C. He, W. Feng, W. Wang, X. Zhou, Z. Yin, L. Chen, H. Wang and X. Mo, *J. Mater. Chem. B*, 2013, **1**, 4601–4611.
- B. Song, C. Wu and J. Chang, *Acta Biomater.*, 2012, **8**, 1901–1907.
- H. Qianjun, G. Yu, Z. Lingxia, Z. Zhiwen, G. Fang, J. Xiufeng, L. Yaping and S. Jianlin, *Biomaterials*, 2011, **32**, 7711–7720.
- A. Malhotra, X. Zhang, J. Turkson and S. Santra, *Macromol. Biosci.*, 2013, **13**, 603–613.
- S. Yan-Tao, C. Hong-Yun, G. Yi, N. Hai-Ming, C. Wei, C. Qiang, C. Bao-Hua, S. Xiao-Dan, Y. You-Wei and L. Heng-De, *Mater. Chem. Phys.*, 2010, **120**, 193–198.
- Y.-J. Yang, X. Tao, Q. Hou, Y. Ma, X.-L. Chen and J.-F. Chen, *Acta Biomater.*, 2010, **6**, 3092–3100.
- H. Kim, L. Che, Y. Ha and W. Ryu, *Mater. Sci. Eng., C*, 2014, **40**, 324–335.
- Y. C. Ou, F. Yang and Z. Z. Yu, *J. Polym. Sci., Part B: Polym. Phys.*, 1998, **36**, 789–795.
- C. G. L. Khoo, S. Frantzich, A. Rosinski, M. Sjöström and J. Hoogstraate, *Eur. J. Pharm. Biopharm.*, 2003, **55**, 47–56.
- B. Duan, X. Yuan, Y. Zhu, Y. Zhang, X. Li, Y. Zhang and K. Yao, *Eur. Polym. J.*, 2006, **42**, 2013–2022.
- S. H. Pangburn, P. V. Trescony and J. Heller, *Biomaterials*, 1982, **3**, 105–108.
- N. Bhardwaj and S. C. Kundu, *Carbohydr. Polym.*, 2011, **85**, 325–333.
- B. N1, D. Edmondson, O. Veiseh, F. A. Matsen and M. Zhang, *Biomaterials*, 2005, **26**, 6176–6184.
- O. Tsigkou, L. L. Hench, A. R. Boccaccini, J. M. Polak and M. M. Stevens, *J. Biomed. Mater. Res., Part A*, 2007, **80**, 837–851.
- G. Toskas, C. Cherif, R. D. Hund, E. Laourine, B. Mahltig, A. Fahmi, C. Heinemann and T. Hanke, *Carbohydr. Polym.*, 2013, **94**, 713–722.
- A. L. Boskey, *J. Cell. Biochem.*, 1998, **30–31**, 83–91.
- M. Bosetti, L. Zanardi, L. Hench and M. Cannas, *J. Biomed. Mater. Res., Part A*, 2003, **64**, 189–195.